




Surface engineered Tb and Co co-doped BiFeO₃ nanoparticles for enhanced photocatalytic and magnetic properties

Ashalata Puhan¹, Bhavya Bhushan¹, Sher Singh Meena², Arpan Kumar Nayak^{3,*} , and Dibyanjan Rout^{1,*}

¹ School of Applied Sciences (Physics), KIIT University, Bhubaneswar 751024, India

² Solid State Physics Division, Bhabha Atomic Research Centre, Mumbai 400085, India

³ Department of Physics, School of Advanced Sciences, Vellore Institute of Technology, Vellore 632014, India

Received: 18 November 2020

Accepted: 8 February 2021

Published online:
27 February 2021

© The Author(s), under exclusive licence to Springer Science+Business Media, LLC part of Springer Nature 2021

ABSTRACT

Controlled synthesis pure-phase Bi_{0.98}Tb_{0.02}Fe_{1-x}Co_xO₃ (BTFCO, $x = 0.01, 0.03, 0.05$ and 0.07) nanoparticles with rhombohedral structure using a facile sol-gel method opens the doors to robust their magnetic and photocatalytic properties significantly. The microstructure analysis revealed improvement in the surface morphology with a decrease of average particle size from 64 to 38 nm. No mixed valance state of iron detected for any sample, which is confirmed by Mössbauer spectra. The saturation magnetization and remnant magnetization were increased dramatically from 0.802 and 0.118 emu/g for BFO to 2.261 and 0.737 emu/g, respectively by Tb, Co co-doping. The enhancement of the magnetic property is attributed to the breakdown of spin cycloidal structure, spin canting, and uncompensated spin on the surface of nanoparticles. Furthermore, the as-synthesized samples are highly effective for rhodamin B (RhB) degradation under visible light irradiation, and the possible photocatalytic mechanism discussed in detail. Bi_{0.98}Tb_{0.02}Fe_{0.93}Co_{0.07}O₃ nanoparticles exhibit the best photocatalytic activity owing to their larger specific surface area, lower band gap, and reduced average particle size. Besides, 1.2% efficiency retention for the degradation of RhB dye using BTFCO7 after the 20th cycle suggests a potential candidate to address the current scenario in the environmental remediation technology.

Address correspondence to E-mail: aknayakju@gmail.com; arpankumar.nayak@vit.ac.in; dibyanjanr@gmail.com; droutfpy@kiit.ac.in

1 Introduction

Multiferroics have attracted mounting interest in the past few years due to their unique magnetoelectric coupling [1]. It encourages researchers to explore promising multifunctional device applications including spintronics, information storage, sensing, actuator, and photocatalysis [2, 3]. Among all of the multiferroics, magnetoelectric bismuth ferrite (BiFeO_3 , referred to as BFO) is the most promising candidate for multifunctional device applications because of its lofty Curie ($T_C \sim 1103$ K) and Neel temperature ($T_N \sim 643$ K) [4]. BFO is the only single-phase multiferroic material that reveals both ferroelectricity and antiferromagnetism at room temperature [5]. Generally, BFO exhibits a rhombohedrally distorted perovskite ABO_3 structure, in which A-site and B-site lead to electric and magnetic ordering, respectively [6, 7]. The antiferromagnetic nature of BFO is due to the presence of cycloidal spin structure with zero net magnetic moment. The magnetic property of BFO can be enhanced using transition-metal ions as a dopant to Fe^{3+} site. Doping of transition-metal ions distorts in the lattice structure, modifies cycloidal spin structures and facilitates the improvement of the magnetic behaviour of BFO. Besides, BFO considered as a potential candidate for the development of wastewater treatment due to its low cost, small band gap (2.1–2.7 eV), lead-free nature, efficient charge-carrier separation, high chemical stability, and saturation polarization ($\sim 90 \mu\text{C}/\text{cm}^2$) [8, 9]. The relatively narrow band gap of BFO increases the light absorption efficiency in the visible region of the electromagnetic spectrum, enhancing the degradation efficiency of organic pollutants under visible light irradiation [10, 11]. Moreover, the ferroelectric properties of BFO can further help to improve the surface reactivity as well as the charge-separation efficiency of the photogenerated charges [12]. Various synthesis techniques and doping with suitable ions in A-site/B-site or both A- and B-sites adopted as versatile tools for the enhancement of the photocatalytic activity and magnetic properties of BFO [6, 13]. In this regard, doping with foreign atoms, either trivalent rare-earth ions (such as Ho, La, Eu, Sm, Gd, Dy, Tb etc.) [7, 14–17] or divalent alkali earth ions (i.e., Ca, Ba, and Sr) [18–22], in the Bi-site and transition-metal (such as Mn, Cr, Co, Ni, Ti etc.) [23–27] in the Fe-site can improve the magnetic

property as well as photocatalytic performance of BFO. Moreover, it has been reported that the co-doping of rare-earth/alkaline-earth and transition-metal ions to both A- and B-sites can significantly improve the multiferroic properties of BFO [28–32]. In particular, Mao et al. reported a higher magnetization value of 0.535 emu/g and enhanced ferroelectric property for rare-earth and Cobalt-doped BFO ($\text{Bi}_{0.95}\text{Ln}_{0.05}\text{Fe}_{0.95}\text{Co}_{0.05}\text{O}_3$ where $\text{Ln} = \text{La}, \text{Pr}$) nanoparticles [29]. In another study, the enhanced magnetic and ferroelectric properties along with the reduced leakage current were inspected on a La, Co co-doped BFO thin film by Yang et al. [30]. The improved ferroelectric property with reduced leakage current by a Tb, Cr co-doping BFO thin film was investigated by Dong et al. [31]. On the other hand, co-doping has also a large impact on photoreactivity [33]. Dopants act like shallow traps for electrons and holes, which decreases the recombination rate and increase the photo-generated charge-carrier lifetime, resulting in the improved photocatalytic behavior of co-doped BFO [33]. Recently, Irfan et al. have observed an improved photocatalytic activity for the detoxification of Congo red (CR) dye using the as-synthesized La^{3+} and Se^{4+} co-doped BFO [33]. Thus, the synthesis of co-doped nanoparticles is proven to tailor the multiferroic properties as well as the photocatalytic activity of BFO under visible light irradiation. Therefore, it is highly desirable to synthesize co-doped BFO nanoparticles with more suitable dopants to achieve higher multiferroic properties as well as enhanced photocatalytic performances.

Herein, for the first time, we tried with a new combination of elements Tb and Co co-doping at A- and B-sites of BFO [$\text{Bi}_{0.98}\text{Tb}_{0.02}\text{Fe}_{1-x}\text{Co}_x\text{O}_3$ (BTFCO, $x = 0.01, 0.03, 0.05$ and 0.07)] nanoparticles using the sol-gel technique. The effect of co-doping on the structural, optical, electrical, and magnetic properties along with the photocatalytic removal of organic pollutants compared to pure BFO explored. Tb was chosen here as a suitable dopant to the Bi-site because of its comparable electronegativity and smaller ionic radius 0.923 \AA (Tb^{3+}) as compared to 1.17 \AA (Bi^{3+}). So, a large structural distortion as expected from Tb substitution and the spiral spin structure of BFO can be destroyed by the doping of the Tb^{3+} ion due to its large magnetic moment, which will enhance the overall property. On the other hand, cobalt doping to the Fe^{3+} site will further enhance the magnetic property of BFO. Doping with Tb and Co may reduce

the particle size, which have a greater influence on the magnetic and photocatalytic properties. The reduction of particle size can improve the magnetic property by suppressing the spin cycloidal structure. On the other hand, the diminished particle size may improve the nanoparticles surface area leading to the enhancement of the photocatalytic and magnetic properties. Hence, the motivation of the present investigation is to co-dope the Tb and Co on the Bi and Fe sites of pure BFO as well as to study the doping effect on the magnetic and photocatalytic properties.

2 Results and discussion

2.1 Structural analysis

Figure 1a demonstrates the powder X-ray diffraction (XRD) patterns of pure BFO and $\text{Bi}_{0.98}\text{Tb}_{0.02}\text{Fe}_{1-x}\text{Co}_x\text{O}_3$ ($x = 0.01, 0.03, 0.05, \text{ and } 0.07$) powders. The intense Bragg features suggest the crystalline nature of the samples, and the obtained pattern well matched with the rhombohedral structure and the R3c space group (JCPDS card No. 00-071-2494). [4] All of

the samples show pure phase, i.e., no additional impurity phases were detected in any X-ray diffraction (XRD) peaks by co-doping of Tb and Co to BiFeO_3 . Further, the enlarged characteristic peak in the 2θ range of $31\text{--}33^\circ$ shown in Fig. 1b. It is noteworthy that with increasing Co concentration, there is a prominent shift of peaks toward higher 2θ , proposing modification of lattice parameters due to doping of a smaller-ionic-radii dopant Tb^{3+} (0.923 Å) and Co^{2+} (0.580 Å) to Bi^{3+} (1.17 Å) and Fe^{3+} (0.645 Å) sites respectively. The shifting may be attributed to the compressive structural lattice distortion by doping of foreign elements into BiFeO_3 [34]. Further, the unit cell parameters (a , c , and V) calculated using X'Pert HighScore and UnitCell software programs found to decrease with an increase in doping concentration (Table 1). The reduction of lattice parameters may be ascribed to the dumping of the axial bonds for the octahedral BiFeO_3 by Tb and Co co-doping. This change in lattice parameter values further evidenced the structural distortion. Similar observations of the lattice parameters were reported by Anju et al. in Ba, Co co-doped BiFeO_3 [35]. Moreover, the broadening of the characteristic peaks [(104) and (110)] (Fig. 1b) indicates an increase in the

Fig. 1 XRD pattern of pure and Tb, Co co-doped BiFeO_3 nanoparticle in 2θ ranges of **a** $20\text{--}80^\circ$, **b** $31\text{--}33^\circ$ with Gaussian Peak fit

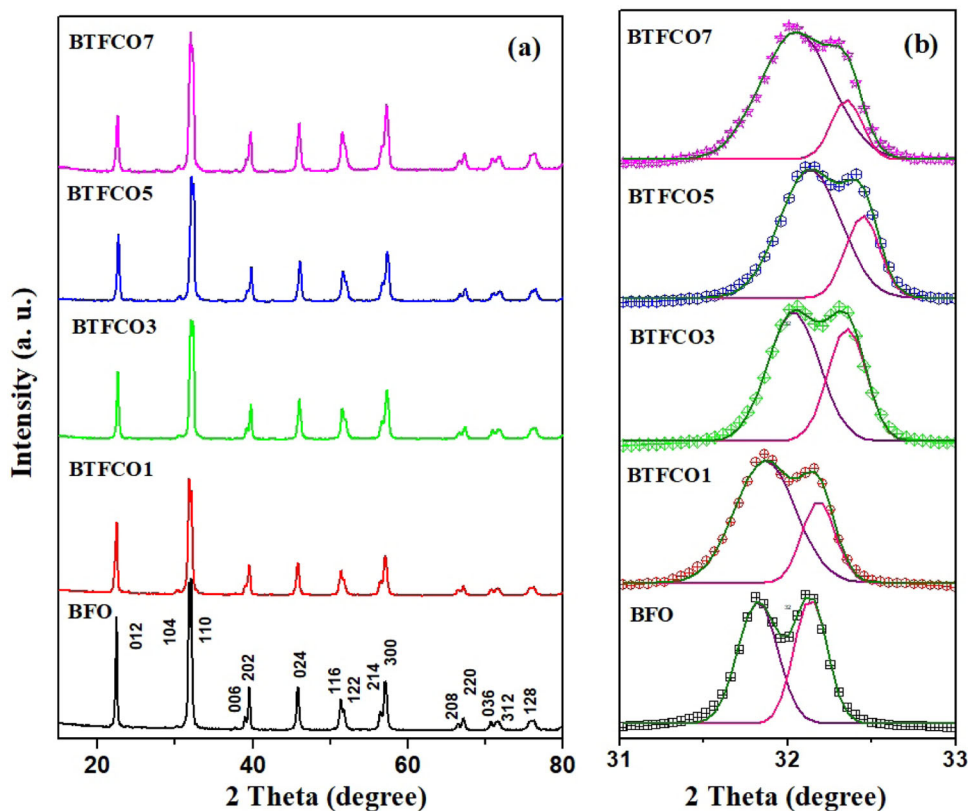


Table 1 Structural parameters of pristine and Tb, Co co-doped BiFeO₃ nanoparticles

Samples	Crystallite size (nm)	Strain	<i>a</i> (Å)	<i>c</i> (Å)	<i>V</i> (Å) ³	Tolerance factor	<i>c/a</i> ratio
BFO	50.630	0.310	5.576	13.861	373.342	0.881	2.485
BTFCO1	49.530	0.341	5.557	13.826	369.740	0.888	2.487
BTFCO3	43.560	0.360	5.534	13.772	365.189	0.889	2.488
BTFCO5	37.401	0.480	5.530	13.765	364.587	0.889	2.489
BTFCO7	35.102	0.542	5.518	13.732	362.141	0.890	2.488

lattice strain and a decrease in the crystallite size [36]. The crystallite size and the lattice strain were calculated by single-line profile analysis (SLPA) considering two highest-intensity peaks (104 and 110), given in Table 1. The crystallite size found to decrease from 50.63 to 35.10 nm, and the lattice strain increased from 0.31 to 0.54 for BFO and BTFCO7, respectively (Table 1), which is the evidence of broadening the characteristic peaks [34]. The raise in lattice strain may be due to the mismatch of ionic size for the host and dopant ions. Moreover, further increasing the doping concentration of Co to 9%, some impurity peaks were observed, including pure BFO peaks (XRD not shown). Therefore, we chose BTFCO7 (7% doping of Co) as the best sample and did not increase the Co concentration. A similar observation of the impurity phase in Ba_{0.1}Co_{0.06}BFO ceramic was also reported by Xi et al. [37].

In addition, the Goldsmith tolerance factor was calculated using the relation $T = \frac{R_A + R_O}{\sqrt{2}(R_B + R_O)}$ by taking the ionic radii reported by Shannon [38]. *T* factor was measured as smaller than one (0.88 to 0.89), suggesting the lattice distortion due to compressive strain acting on the Fe–O or Bi–O bond of BiFeO₃. This is further supported by the change in the *c/a* ratio observed with Tb, Co co-doping.

2.2 Morphology

Figure 2 shows the field emission scanning electron microscopy (FESEM) micrographs of pure and Tb, Co co-doped BFO nanoparticles. Both pristine and Tb, Co co-doped samples reveal quasi-spherical morphology with densely packed and homogeneously distributed particles. The average particle size was 64, 56, 51, 45, and 38 nm for BFO, BTFCO1, BTFCO3, BTFCO5, and BTFCO7, respectively. The inset digital photographs (right-hand-side bottom corner, Fig. 2) show a gradual color change in the synthesized nanoparticles with increasing Co-doping content. It noted that the average particle size found to decrease

with an increase in dopant concentration. The diminution of particle size ascribed to the slower growth rate because of co-doping [39]. The consequences well correlated with the crystallite size analyzed using Scherer formula, as shown in Table 1.

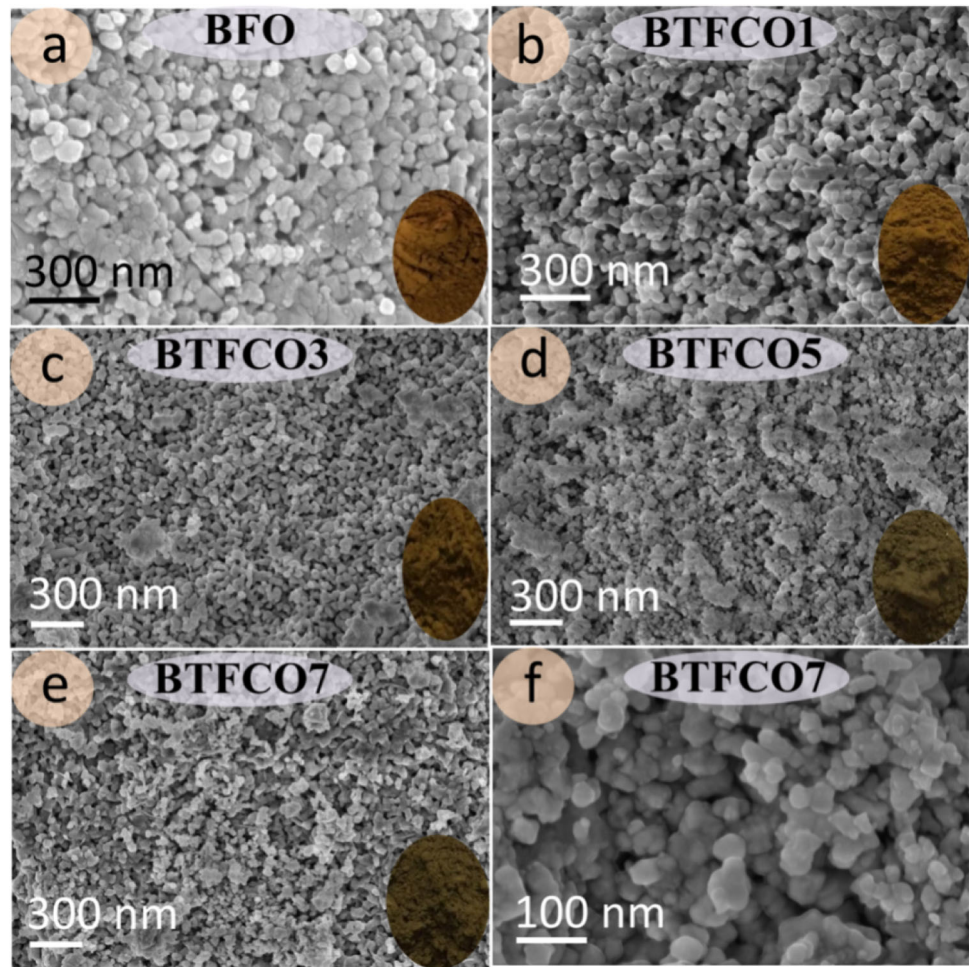
2.3 Microstructure

The microstructure analysis further elucidated using transmission electron microscopy (TEM). Figure 3 shows the TEM, selected area electron diffraction (SAED), and high-resolution TEM (HRTEM) micrographs of BFO and BTFCO7 nanoparticles. The micrographs (Fig. 3a and d) display spherical particles with average particle sizes of 61 nm (BFO) and 37 nm (BTFCO7). The reduction of particle size (nearly 1.65 times) after co-doping correlated with the FESEM and XRD results. The SAED images demonstrated ring pattern well-defined spots for BFO and the BTFCO7. It suggests a better crystalline nature of the samples after doping [16]. Again, the inter planer lattice spacing calculated to be 2.86 Å (BFO) and 2.9 Å (BTFCO7) corresponding the (110) plane, which is the most intense bragg peak in the rhombohedral-phase BFO (JCPDS 86-1518) [40].

2.4 Dielectric properties

The effect of co-doping on the dielectric properties as a function of frequency studied at room temperature. Figure 4 displays a decrease in the dielectric permittivity (ϵ) and dielectric loss tangent ($\tan\delta$) with increasing frequency from 0.1 kHz to 1 MHz, which can be explained by dielectric relaxation [41]. At a low frequency, the dipoles are capable of following the applied electric field. However, at a higher frequency, the dielectric permittivity is weakly dependent on frequency. Therefore, the dielectric permittivity of pure and doped BFO depends on the ferroelectric domain rather than an electric dipole [42]. Moreover, the dielectric permittivity increased gradually from 56 (BFO) to 95 (BTFCO7) at 10 kHz

Fig. 2 FESEM micrographs of **a** pure BFO and $\text{Bi}_{0.98}\text{Tb}_{0.02}\text{Fe}_{1-x}\text{Co}_x\text{O}_3$ with **b** $x = 0.01$, **c** $x = 0.03$, **d** $x = 0.05$, and **e, f** $x = 0.07$. The right corner bottom insets of **a–e** show the digital photographs of as-synthesized powder samples



with an increase in Co concentration, which may be ascribed to the structural distortion via doping with smaller-ionic-radii dopants like Tb and Co. However, the dielectric loss (Fig. 4b) found to decrease due to the formation of oxygen vacancies by doping Co^{2+} to the Fe^{3+} site [43]. A higher dielectric loss with doping of Co to the Fe site of BiFeO_3 was also inspected by Varshney et al. [42].

2.5 Leakage current study

The leakage current density (J) was recorded as a function of electric field (E) to study the conduction mechanism of all of the products. Figure 5a shows an increasing trend of current density with an increase in the applied electric field. Besides, the value of J found to decrease for BTFCO1 nearly 1st order, which might be due to the suppression of oxygen vacancy. However, with further increase in the Co concentration, it increased sharply up to 2 orders

compared to pure BFO, which can be well correlated with the increased $\tan\delta$ value due to the formation of oxygen vacancies resulting from charge imbalance by doping of Co^{2+} to the Fe^{3+} site [44]. A similar trend observed in Ba, Co co-doped BFO ceramics, as reported by Xi et al. [37].

In get more information about the conduction mechanism, $\log J$ vs. $\log E$ plotted and the slopes were resolved by a linear fit shown in Fig. 5b. Based on the slope values, the conduction mechanism generally considered to be Ohmic for slope ~ 1 , space charge-limited conduction (SCLC) for slope ~ 2 , and Poole–Frenkel or Schottky for slope value > 2 [45, 46]. In this report, the slopes were measured to be 0.835, 0.85, 0.99, 1.00, and 0.97 for BFO, BTFCO1, BTFCO3, BTFCO5, and BTFCO7, respectively, suggesting Ohmic conduction for all of the samples.

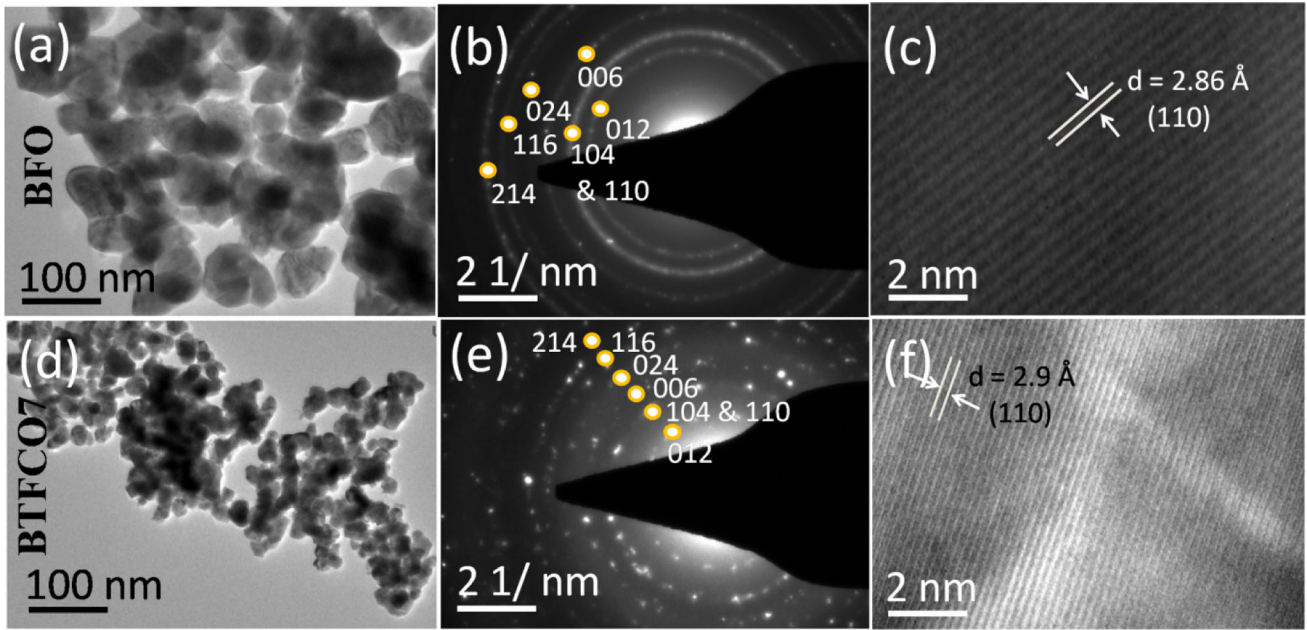


Fig. 3 TEM micrographs of **a** pure BFO, and **d** BTFCO7; SAED pattern of **b** Pure BFO, and **e** BTFCO7; and HRTEM micrographs of **c** pure BFO, and **f** BTFCO7

Fig. 4 Room temperature **a** ϵ , and **b** $\tan \delta$ as a function of frequency for BFO and co-doped BFO nanoparticles

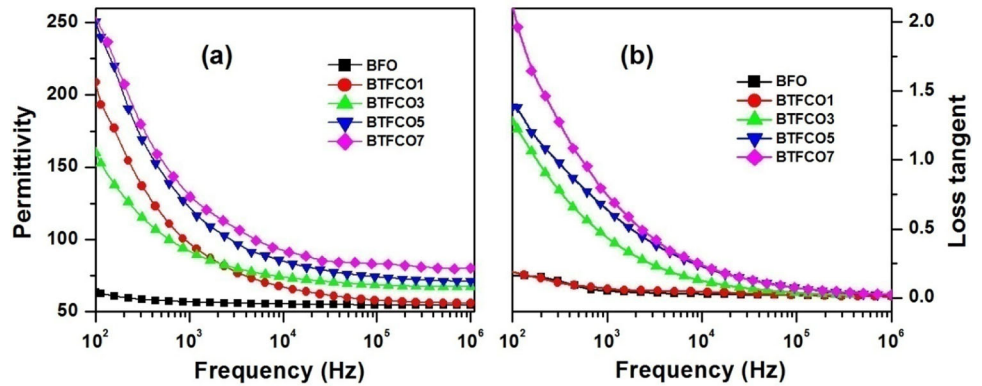
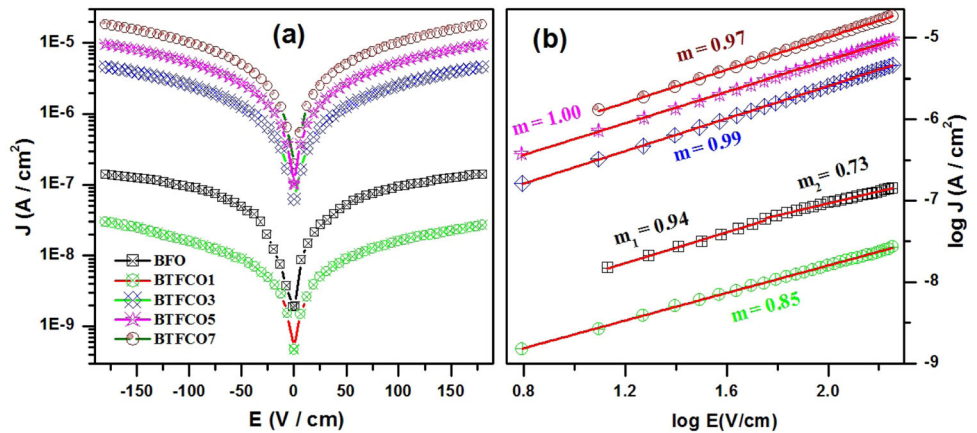


Fig. 5 **a** J vs. E at room temperature, and **b** $\log J$ vs. $\log E$ of pure and Tb, Co co-doped BiFeO₃ nanoparticles



2.6 Magnetic properties

As shown in Fig. 6, the magnetic hysteresis loop was recorded at room temperature to study the influence of Tb and Co co-doping on the magnetic behavior of BiFeO₃ nanoparticles. All of the samples revealed a sizable hysteresis loop with a finite value of the coercive field (H_c), remanent magnetization (M_r), and saturation magnetization (M_s). The M_s value increased from 0.8 (BFO) to 2.26 emu/g (BTFCO7) at an applied field of 10 kOe, and the M_r value increased 6.25 times compared to pure BFO by Tb, Co co-doping, as shown in Fig. 6b. The development of magnetic behavior primarily attributed to the breakdown of the spiral spin structure due to the reduction of the particle size below 62 nm. [47]–[48]. Also, the structural distortion by doping of Tb and Co, as discussed in XRD, may be a reason for the enhanced magnetic property. The structural distortion can influence the Dzyaloshinskii–Moriya (DM) interaction, which leads to the spin canting and suppresses the cycloidal spin structure arrangement, resulting improved magnetic properties [49]. Furthermore, the doping of Co²⁺ to the Fe³⁺ site can create oxygen vacancy due to charge imbalance and can enhance the magnetic behavior of the doped nanoparticles [50]. The surface-to-volume ratio increased as the volume decreased (discussed in the XRD result), and the surface area increased (discussed later in BET section) with an increase in the Co concentration via doping. Therefore, extra uncompensated spins on the surface of the nanoparticles can play a crucial role in improving the magnetic property [51]. Also substitution of magnetic active transition-metal ion Co might enhance the magnetic behavior of the as-synthesized samples [52]. The Maximum values of

$M_s = 0.535$ emu/g and $M_r = 0.025$ emu/g observed by La, Co co-doping as reported by Mao et al. [29].

Moreover, a drastic improvement in the coercive magnetic field from 122.84 to 909.14 Oe was observed by the doping of Tb and Co simultaneously (inset in Fig. 6b). The detailed particle size, dielectric constant, dielectric loss, leakage current, and magnetic parameters of pure and Tb, Co co-doped BFO samples presented in Table 2. The enhanced coercive field of the doped nanoparticles was ascribed to the improved magneto-crystalline anisotropy and magneto-elastic anisotropy by an increase in the Co concentration [43]. Recently, Anju et al. have reported an enhanced M_s and M_r values of 0.425, and 0.22 emu/g for Bi_{0.8}Ba_{0.2}Fe_{0.95}Co_{0.05}O₃ nanoparticles, respectively [35]. Godra et al. found an optimum amount of magnetization ($M_s = 1.7$) by co-doping of Ba and Co to the BFO system [50]. In the present work, a considerable improvement in the magnetic property by Tb, Co co-doping in BiFeO₃ nanoparticles was evidenced compared to several previous reports (Table S1, Supporting Information (SI)) based on various co-doped BFO samples. The enhanced magnetic property of the as-synthesized BiFeO₃ nanoparticles by Tb, Co co-doping, makes it suitable for application in multiple types of magnetic sensor devices.

2.7 Mossbauer analysis

Room-temperature Mössbauer spectra captured to identify the oxidation state of iron by doping. Figure 7 exhibits the Mössbauer spectra of BiFeO₃ and Tb, Co co-doped BiFeO₃ nanoparticles operated at a constant acceleration mode in transmission geometry with 25 mCi of the Co [56] source in the Rh matrix. All of the samples well fitted with two sextets (red

Fig. 6 **a** Room-temperature M – H hysteresis loop of pure and Tb, Co co-doped BiFeO₃ nanoparticles. **b** Variation of magnetic parameters (M_s , M_r and H_c) with doping concentration of cobalt

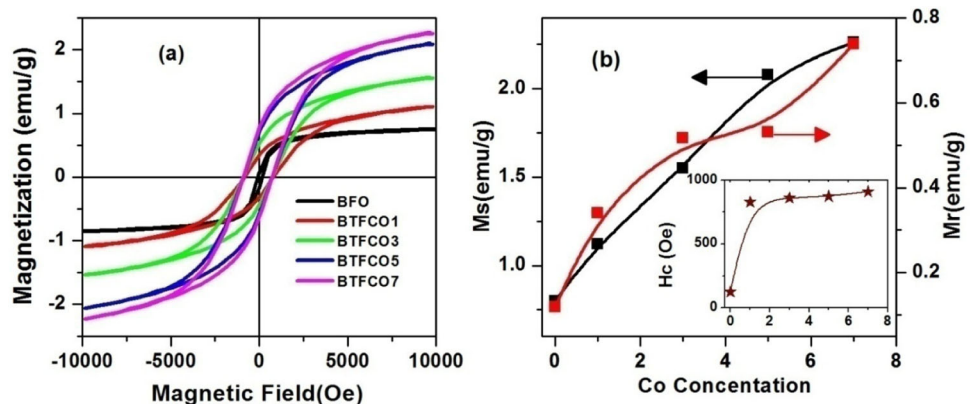


Table 2 Variation of particle size, dielectric constant, dielectric loss, leakage current and magnetic parameters of pure and Tb, Co co-doped BFO nanoparticles

Samples	Particle size (nm)	Dielectric constant (at 10^4 Hz)	Dielectric loss (at 10^4 Hz)	Leakage current (A/cm ²)	M_r (emu/g)	M_s (emu/g)	H_c (emu/g)
BFO	64	55	0.028	1.99×10^{-7}	0.118	0.802	122.841
BTFCO1	56	68	0.056	2.62×10^{-8}	0.341	1.120	826.493
BTFCO3	51	74	0.133	4.53×10^{-6}	0.517	1.550	860.692
BTFCO5	45	85	0.257	1.87×10^{-5}	0.531	2.083	872.094
BTFCO7	38	96	0.259	9.8×10^{-5}	0.737	2.261	909.143

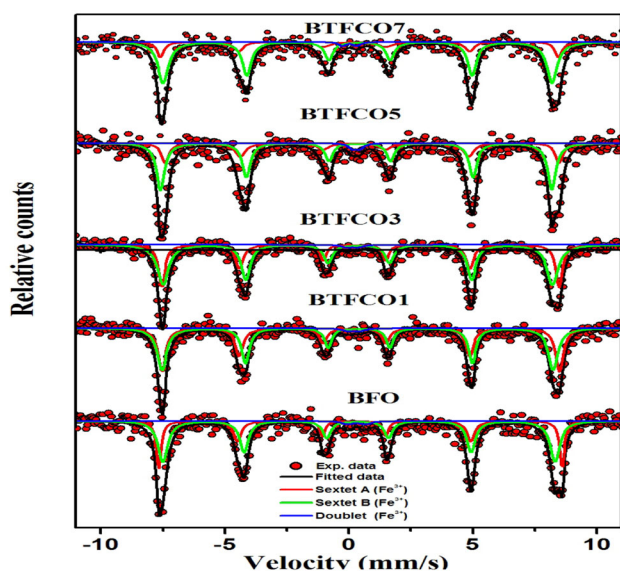


Fig. 7 Room-temperature Mössbauer spectra pure and Tb, Co co-doped BiFeO₃ nanoparticles

and green colors) and one doublet (blue color). The observed hyperfine parameters from the fitting are tabulated in Table 3. A doublet shown in the samples may be a super paramagnetic doublet due to smaller particle size.

Generally, the oxidation state of iron is confirmed by the isomer shift values [53]. The isomer shift values of all of the pure and doped samples were found to be in the range of 0.318–0.377 for both sextets A and B. Further, the isomer shift values for the doublet were measured to be in the range of 0.028–0.409. All isomer shifts for Sextet A, Sextet B, and Doublet were confirmed the 3+ oxidation state of iron [47]. Diminutive values of isomer shift data point toward the fact that the local environment of iron did not get changed by Tb and Co co-doping. Furthermore, a negative value of quadruple splitting (ΔE_Q) was

observed for sextet B corroborated to the G-type antiferromagnetic nature of BFO. However, the ΔE_Q value for sextet A observed to be significantly superior to sextet B, which confirmed the ferromagnetic nature of the co-doped BiFeO₃ nanoparticles.

2.8 N₂ adsorption–desorption isotherms

The specific surface area was calculated to measure the exact surface area of the samples using the Brunauer–Emmett–Teller (BET) method. In general, a photocatalyst with a larger surface area induces a higher photoactivity. Hence, the N₂ adsorption–desorption isotherm measurement along with Barrett–Joyner–Halenda (BJH) pore size distribution was employed to study the effect of co-doping on the surface area and total pore volume of BFO nanoparticles. Figure 8 shows that the N₂ adsorption–desorption isotherms are type IV isotherms, where the starting region is nearly related to type II isotherm according to the Brunauer classification, suggesting mesoporous material [54, 55]. A Similar isotherm trend was observed by Irfan et al. in Gd³⁺ and Sn⁴⁺ co-doped BFO nanoparticles [55]. The specific surface area (total pore volume) was estimated to be 33.3 m²/g (0.094 cm³/g), 43.6 m²/g (0.141 cm³/g), 49.8 m²/g (0.149 cm³/g), and 56 m²/g (0.166 cm³/g) for pure BFO, BTFCO3, BTFCO5, and BTFCO7, respectively. It observed that BTFCO7 has a larger specific surface area and higher pore volume than other samples, which attributed to the smaller particle size. Hence, the results suggested that the surface area enhanced with an increase in the Co content at BTFO, which might accelerate the photocatalysis process for the degradation of the RhB dye with superior performance using co-doped BFO nanoparticles.

Table 3 Hyperfine parameters of as-synthesized pure and Tb, Co co-doped BiFeO₃ nanoparticles

Sample	Fe sites	Isomer shift (δ) mm/s ± 0.01	Quadrupole splitting (ΔE_Q) mm/s ± 0.01	Hyp. Mag field (H_{hf}) Tesla ± 0.06	Relative Area, R_A (%)	Line width (Γ) mm/s ± 0.05	Goodness of fit (χ^2)
BFO	Sextet A (Fe ³⁺)	0.340	0.330	49.760	33.701	0.337	1.146
	Sextet B (Fe ³⁺)	0.375	− 0.010	49.100	64.801	0.465	
	Doublet (Fe ³⁺)	0.409	0.247	–	1.501	0.501	
BTFCO1	Sextet A (Fe ³⁺)	0.347	0.250	49.701	46.403	0.375	1.001
	Sextet B (Fe ³⁺)	0.372	− 0.051	48.910	52.302	0.467	
	Doublet (Fe ³⁺)	0.188	0.438	–	1.302	0.501	
BTFCO3	Sextet A (Fe ³⁺)	0.342	0.237	49.681	29.501	0.318	1.023
	Sextet B (Fe ³⁺)	0.374	− 0.040	48.690	69.401	0.547	
	Doublet (Fe ³⁺)	0.132	0.424	–	1.101	0.501	
BTFCO5	Sextet A (Fe ³⁺)	0.377	0.314	49.242	38.903	0.366	0.980
	Sextet B (Fe ³⁺)	0.359	− 0.139	48.901	59.702	0.412	
	Doublet (Fe ³⁺)	0.287	0.284	–	1.402	0.350	
BTFCO7	Sextet A (Fe ³⁺)	0.318	0.214	49.770	31.701	0.340	1.091
	Sextet B (Fe ³⁺)	0.383	− 0.070	48.591	67.401	0.390	
	Doublet (Fe ³⁺)	0.028	0.571	–	0.902	0.350	

2.9 Optical analysis

Figure 9 shows the UV–Visible absorption spectra of BiFeO₃ (BFO) and Tb, Co co-doped BFO nanoparticles. All of the samples exhibit absorbance peaks (Fig. 9a) in the wavelength range of 400–550 nm. This indicates that the band gap is in the visible region of the electromagnetic band. A shifting of absorbance spectra toward higher wavelength (red shift) was observed for Tb, Co co-doped BFO nanoparticles. The red shift of absorbance peaks may be due to the higher lattice strain and smaller particle size, as reported in the XRD and TEM data [56]. Moreover, the band gap of pure and co-doped BFO nanoparticles was measured from the point of inflection at the first derivative of absorption spectra and found to be decreased from 2.33 to 1.87 eV for BFO to Tb, Co co-doped BTFO (Fig. 9b) [57]. Especially this reduced band gap value is much lesser than in the previously reported BFO-based materials [3, 58, 59]. The smallest band gap of 1.87 eV observed for 7% Co-doped BTFO (BTFCO7) indicated a semiconducting behavior of the sample. Further, the band gap of pure BFO and co-doped BFO nanoparticles was measured using the Tauc equation $[(\alpha h\nu)^2 \text{ versus } h\nu]$ for comparison [60]. From the Tauc plot (Fig. S1), the band gap was measured to be 2.02, 1.97, 1.7, 1.69, and 1.64 eV for BFO, BTFCO1, BTFCO3, BTFCO5, and

BTFCO7, respectively. This semiconducting behavior may be accredited to the formation of oxygen vacancy, as confirmed by the dielectric and leakage current analysis. Therefore, the smaller band gap of the Bi_{0.9}Tb_{0.02}Fe_{0.93}Co_{0.07}O₃ photocatalyst makes it a potential candidate for degradation of organic dye under visible light irradiation.

Furthermore, the band structure of pure and doped samples was studied by way of electronegativity. The positions of conduction band (CB) and valence band (VB) of the synthesized nanoparticles were calculated using the empirical formula given below [61]

$$E_{\text{CB}} = \chi - E^e - 0.5E_g \quad (1)$$

$$E_{\text{VB}} = E_{\text{CB}} + E_g \quad (2)$$

where E_{VB} stands for the valance band edge potential and E_{CB} represents the conduction band edge potential. E^e demonstrates the energy of free electrons vs. hydrogen scale (~ 4.5 eV) and E_g signifies the optical band gap of synthesized nanoparticles measured from UV–Visible absorption spectra. The electronegativity (χ) of semiconductor was calculated using the following Eq. [61]

$$\chi = \left[(\chi_{\text{Bi}})^a \times (\chi_{\text{Fe}})^b \times (\chi_{\text{O}})^c \right]^{1/(a+b+c)} \quad (3)$$

Herein, a , b and c depicts the number of atoms existing in the compound. The obtained χ value for

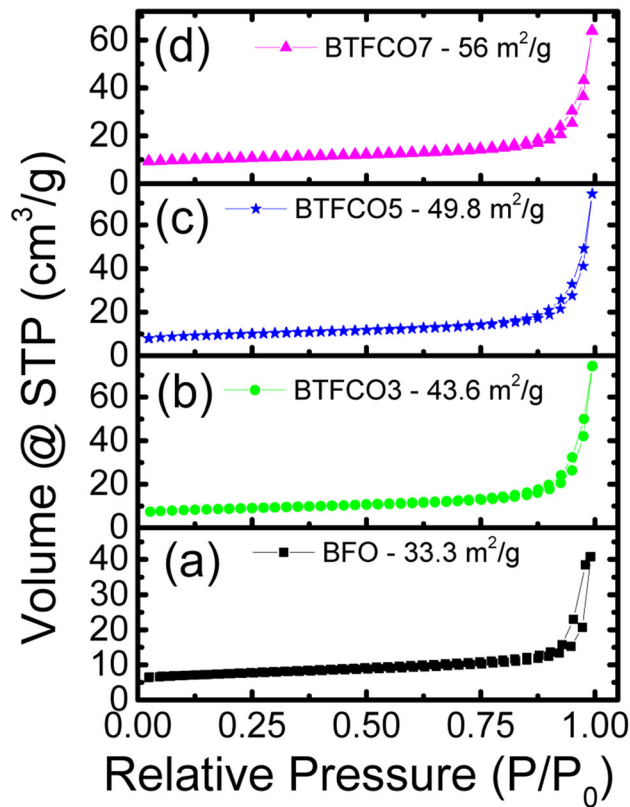


Fig. 8 N₂ adsorption-desorption isotherms of **a** BFO, **b** BTFCO₃, **c** BTFCO₅, and **d** BTFCO₇

BFO was determined to be 5.88 eV. Figure 10 represents the measured band edge (VB, CB) position of pure and Tb, Co co-doped BFO nanoparticles. The valence band edge (E_{VB}) position was found to be 2.55, 2.49, 2.50, 2.35, and 2.32 eV for BFO, BTFCO₁, BTFCO₃, BTFCO₅, and BTFCO₇, respectively and the conduction band edge (E_{CB}) was estimated to be

0.22 eV (BFO), 0.26 eV (BTFCO₁), 0.32 eV (BTFCO₃), 0.40 eV (BTFCO₅), and 0.45 eV (BTFCO₇) respectively versus normal hydrogen electrode (NHE).

2.9.1 Photocatalytic degradation

Photocatalysis technology has widely proven to address the environmental issue for the degradation of organic pollutants [62–64]. The photocatalytic activities of the as-synthesized pure BFO, BTFCO₁, BTFCO₃, BTFCO₅, and BTFCO₇ nanoparticles along with standard P-25 (TiO₂ nanoparticles ~ 21 nm diameter) evaluated for the removal of rhodamine B (RhB) dye under an incident 500 W halogen lamp (visible light) irradiation. TiO₂ is considered as a benchmark photocatalyst under UV light, due to its high photocatalytic activity, excellent physical and chemical stability, low cost, noncorrosive nature, nontoxicity, and high availability in the market. Therefore, we compare the photocatalytic behavior of as-synthesized BFO with standard TiO₂ [65]. Before irradiation, the RhB aqueous solutions (10⁻⁵ mol/L), and the photocatalysts were magnetically stirred for 30 min in the dark to attain the adsorption-desorption equilibrium. Figure 11a reveals the UV-Vis absorption spectra as a function of incident time for RhB aqueous solution ($\lambda_{max} = 554$ nm) in the presence of BTFCO₇ photocatalyst under incident visible light irradiation. The absorbance intensity found to be decreasing (Fig. 11a) with increasing the incident duration, suggesting the photocatalytic degradation of the RhB dye molecule. Figure 11b shows the RhB degradation performance of all samples, including Standard TiO₂ (P-25) by plotting relative

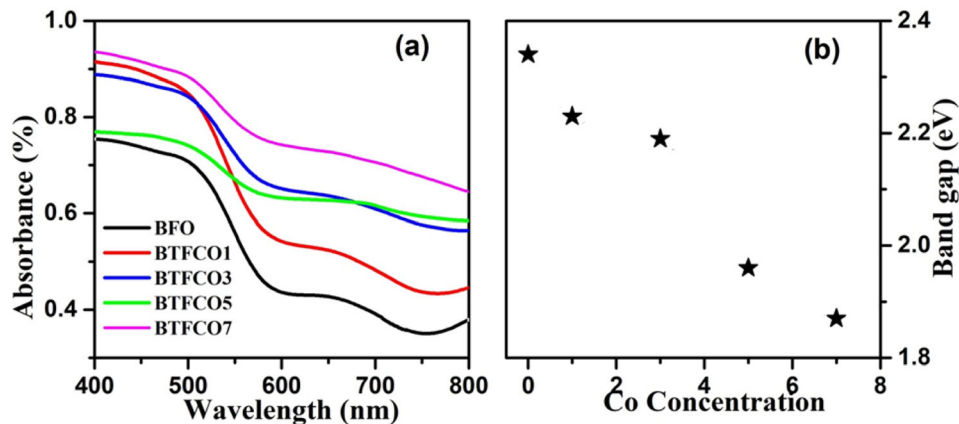
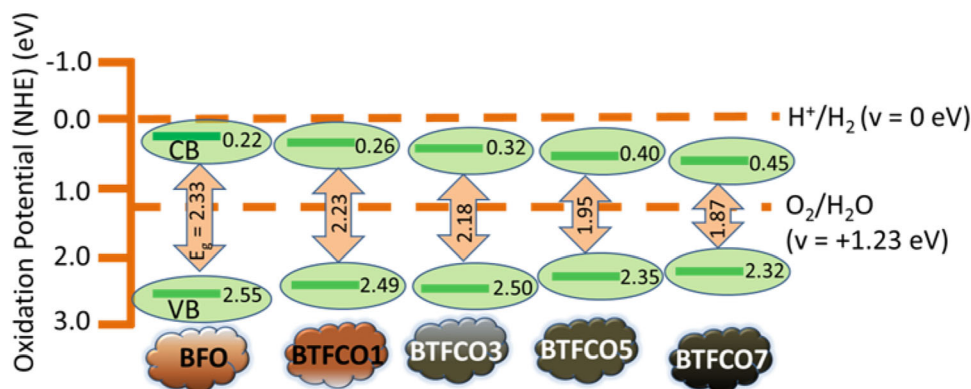


Fig. 9 **a** UV-Visible absorption spectra of pure BFO and Bi_{0.98}Tb_{0.02}Fe_{1-x}Co_xO₃ ($x = 0.01, 0.03, 0.5$ and 0.07) nanoparticles, **b** Plot of band gap as a function of Co concentration

Fig. 10 Schematic representation of measured band edge position (VB and CB) for BFO, BTFCO1, BTFCO3, BTFCO5, and BTFCO7 nanoparticles



concentration (C/C_0) versus time in the dark and under irradiation, where C_0 and C are the initial RhB concentration and RhB concentration after irradiation time, respectively. The photocatalytic degradation efficiency of the RhB dye for pure BFO and Tb, Co co-doped BFO nanoparticles was estimated using equation $(C_0 - C)/C_0 \times 100$. A negligible decrease in the RhB dye concentration (Fig. 11b) for all samples was found under dark conditions. The photocatalytic RhB degradation activity was measured to be in the order of BTFCO7 (92%) > BTFCO5 (84%) > BTFCO3 (79%) > TiO_2 (77.4%) > BTFCO1 (72%) > BFO nanoparticles (70%). The higher photocatalytic performance of BTFCO7 ascribed to its higher surface area, lower band gap, and smaller particle size. The RhB degradation efficiency found to be higher compared to several BFO-based materials (Table S2, SI). Further, the RhB dye degradation rate constant calculated from the slope of the straight-line plot $\ln(C_0/C)$ as a function of irradiation time (Fig. 11c). The reaction rate constant of the RhB dye concentration was estimated to be 0.0145, 0.0151, 0.018, 0.021, 0.029, and 0.0171 min^{-1} for BFO, BTFCO1, BTFCO3, BTFCO5, BTFCO7, and TiO_2 (P-25) nanoparticles, respectively. The pure BFO nanoparticles exhibit the lowest photocatalytic activity compared to doped samples, which attributed to their larger size, lower surface area, and larger band gap. Moreover, both the stability and reusability of the catalyst play a crucial role in industrial application. In this regard, we use our best sample BTFCO7 nanoparticles for several cycles (20 cycles) to study the photocatalytic reproducibility (Fig. 11d). The degradation efficiency of the RhB dye found to be 90.46% (Fig. 11d) for the 20th cycle using BTFCO7 nanoparticles. The negligible decrease in efficiency (1.0%) after 20th cycle observed for the removal of the RhB dye under visible light

using BTFCO7 nanoparticles, which confirms its stability for industrial applications. Moreover, the comparison of nanoparticle based morphology for the degradation of various dyes is shown in Table 4.

The present photocatalytic process mechanism of the RhB dye explained as follows. On irradiating visible light ($> E_g$) over the BTFCO7 catalyst, electrons (e^-) and holes (h^+) produced in the valence band (VB) and conduction band (CB), respectively (Scheme 1). The free electrons in the CB of BTFCO7 nanoparticles ($E_{CB} = +0.45 \text{ V vs. NHE}$) are more positive than $\text{O}_2/^*\text{O}_2^-$ ($E_{CB} = -0.33 \text{ eV vs. NHE}$), suggesting that the electrons cannot reduce the oxygen molecule (O_2) to superoxide radicals ($^*\text{O}_2^-$). Thus, the gathered electrons in the CB of BTFCO7 can transform the adsorbed oxygen molecule to H_2O_2 ($E_{CB} = +0.682 \text{ eV vs. NHE}$) [61]. Then, the produced hydrogen peroxide (H_2O_2) molecules react with free electrons to form hydroxyl radicals ($^*\text{OH}$). Meanwhile, the holes in the VB cannot react with absorbed OH^- and water (H_2O) to generate $^*\text{OH}$ radicals, since the potentials of $^*\text{OH}/\text{OH}^-$ ($E_{VB} = +2.38 \text{ eV vs. NHE}$) and $^*\text{OH}/\text{H}_2\text{O}$ ($E_{VB} = +2.72 \text{ eV vs. NHE}$) are higher than VB potential of BTFCO7 ($E_{VB} = +2.32 \text{ eV vs. NHE}$) [61]. Therefore, the formed hydroxyl radicals ($^*\text{OH}$) would react directly with RhB to produce the final degraded products as H_2O and CO_2 .

3 Conclusions

In summary, single-phase pure and Tb, Co co-doped BiFeO_3 nanoparticles were synthesized by a facile sol-gel technique. The particle size of pure BFO was reduced to 1.68 times by Tb, Co co-doping. Tb, Co co-doped BFO nanoparticles observed a significant

Fig. 11 **a** Changes in UV–Vis absorption spectrum of aqueous RhB solution (1×10^{-5} M) irradiated for different durations with BTFCO7. **b** Photocatalytic degradation efficiency of as-synthesized photocatalysts along with P-25 for comparison. **c** Photocatalytic degradation kinetics of RhB dye with all of the samples. **d** Cyclic stability performance of RhB dye degradation using BTFCO7 nanoparticles for 20 cycles

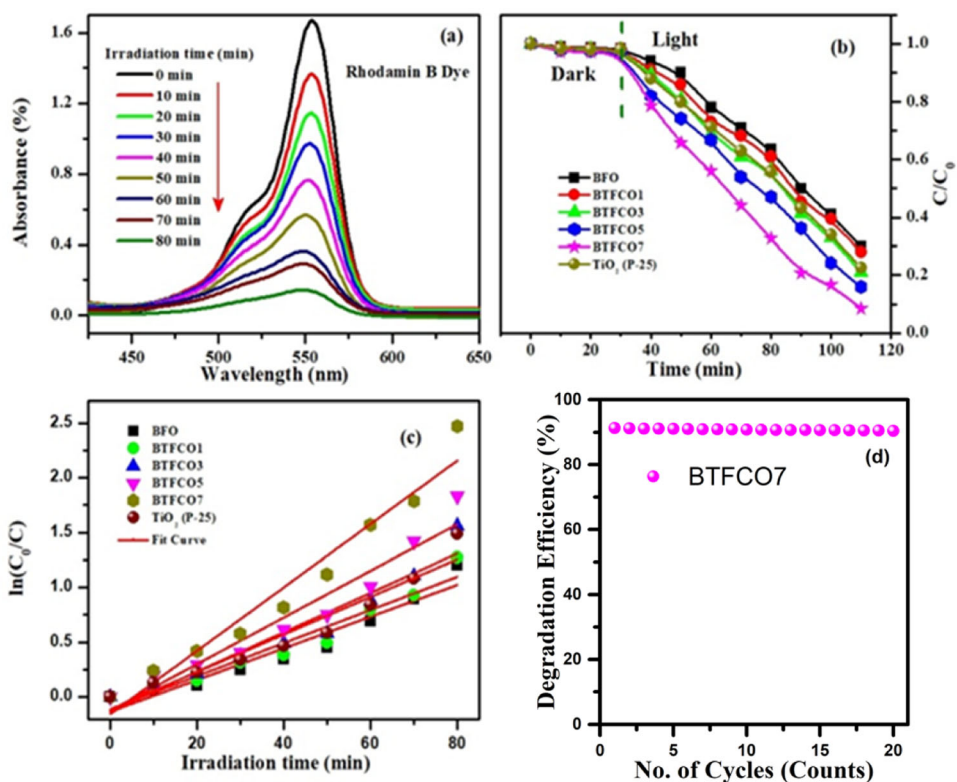


Table 4 The photocatalytic performance of nanoparticles based morphology for the degradation of dyes

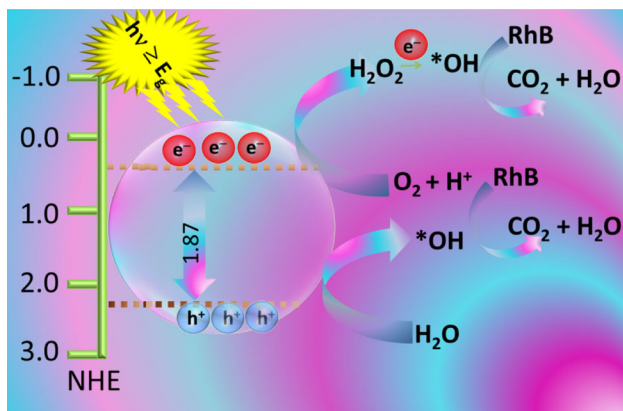
Catalyst name	Synthesis method	Light source	Dye	Degradation efficiency (%)	Reaction rate constant	References
CuO	Solid state thermal decomposition	UV lamp (254 nm)	MB	97	0.018 min^{-1}	67
NiO	Solid state thermal decomposition	UV lamp (254 nm)	MB	97	0.017 min^{-1}	68
Au/TiO ₂	Deposition–precipitation	UV lamp (365 nm)	SO	97	0.006 min^{-1}	69
TiO ₂	Hydrothermal	6 W lamp (365 nm)	MB	97	0.018 min^{-1}	70
N'((E)-benzylidene)-2-(4-(E) hydrazonomethyl)phenoxy)acetohydrazide (H3)	Re-precipitation method	–	–	96.7	–	71
TiO ₂	Modified hydrothermal	UV lamp (254 nm)	MB	96	0.013 min^{-1}	72
In ₂ O ₃	Hydrothermal and thermal treatment	UV light (365 nm)	RhB	88	–	73
BTFCO7	Sol–gel	Halogen lamp (500 W)	RhB	92	0.017 min^{-1}	This work

improvement of the magnetic property with increased saturation magnetization and coercive magnetic field from 0.802 (BFO) to 2.261 emu/g (BTFCO7) and 122.841 (BFO) to 909.143 Oe (BTFCO7), respectively. Further, the remnant magnetization enhanced 6.25 times of pure BFO by Tb, Co co-doping. The isomer shift value obtained from Mössbauer spectra confirms the 3+ oxidation state of iron. Besides, 7% Co-doped BTFCO nanoparticle exhibited a high surface area (56 m²/g) compared to pure BFO. The optical band gap found to be decreasing in co-doped samples. The smaller particle size, larger surface area, and lower band gap make the Bi_{0.98}Tb_{0.02}Fe_{0.93}Co_{0.07}O₃ nanoparticle as a better photocatalytic candidate for degradation of the RhB dye. The degradation efficiency found to be 92% for BTFCO7. The minor reduction in efficiency (1.0%) after the 20th cycle observed for the removal of the RhB dye under visible light using BTFCO7 nanoparticles, which confirmed its stability for industrial applications. Moreover, the improved magnetic property and photocatalytic activity of Tb, Co co-doped BFO nanoparticles makes them a potential candidate for multifunctional device applications.

4 Experimental segments

4.1 Materials synthesis

A facile sol–gel method is used to synthesize pure BiFeO₃ (BFO) and Bi_{0.98}Tb_{0.02}Fe_{1-x}Co_xO₃ (BTFCO) with $x = 0.01, 0.03, 0.5$ and 0.07 nanoparticles, and the compositions are named as BFO, BTFCO1, BTFCO3, BTFCO5, and BTFCO7, respectively (Scheme 2). The



Scheme 1 Schematic diagram for the degradation mechanism of RhB over the BTFCO7 nanoparticles

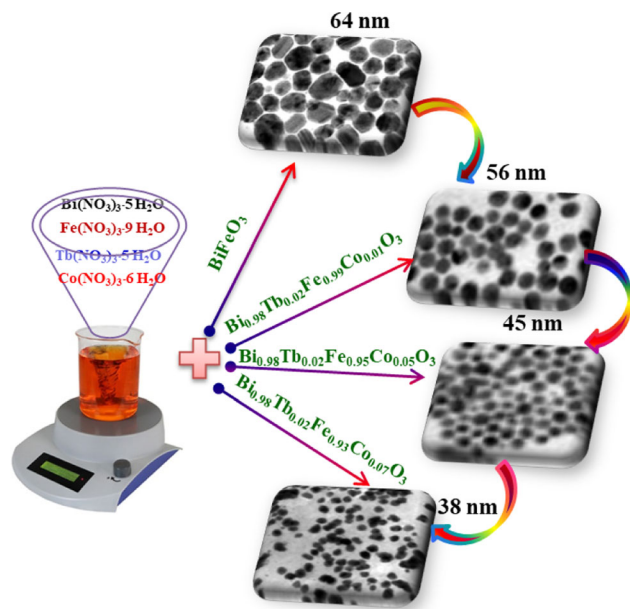
high-purity reagents of Bi(NO₃)₃·6H₂O, Tb(NO₃)₃·5H₂O, Fe(NO₃)₃·9H₂O and Co(NO₃)₂·6H₂O in a stoichiometric ratio were dissolved in ethylene glycol (C₂H₆O₂) with constant stirring at 80 °C for 60 min, then a gel was formed after drying the solution at 80 °C for 10 h in an oven. The prepared gel was preheated at 400 °C for 60 min, grinded using a mortar and pastel and finally, annealed at 550 °C for 60 min. The prepared powders were washed several times using distilled water and isopropanol and dried at 60 °C overnight.

4.2 Characterization

For structural analysis, the samples were characterized by a high-resolution powder X-ray diffractometer using Cu K α radiation (BRUKER D8 ADVANCE) with scanning angle 20–80°. The morphology and microstructural characterization of the powders were obtained by a field emission scanning electron microscope (SIGMA, Carl Zeiss) and high-resolution transmission electron microscope (FEI Tecnai G² 30, Hillsboro, U.S.A) respectively. For the electrical measurements, the green pellets were prepared with thickness (2 mm), diameter (10 mm) and PVA (polyvinyl alcohol (5%)) as a binder and sintered for 60 min at 600 °C in a high temperature Lenton Furnance. Then, both sides of sintered pellets were coated using silver paste. The dielectric properties were studied using a Dielectric/Impedance Alpha-A Analyzer (Novocontrol Broadband). The I – V characteristics were investigated using a Sourcemeter (Keithley, Model No: 2450). Room temperature magnetic (M – H) loops were measured by a Vibrating Sample magnetometer (USA; Model 7404). Mössbauer spectrometer was operated at constant acceleration mode (triangular wave) with transmission geometry. The UV–Vis spectra of the powders were carried out using UV Visible Spectrophotometer (JASCO, V-670 PC). The specific surface area, total pore volume and pore size distribution of the samples were analyzed using a BET surface area analyzer instrument at 77 K (Quantachrome USA).

Acknowledgements

This work was supported by Science and Engineering Research Board (SERB), Department of Science and Technology, Government of India, DST-SERB



Scheme 2 Schematic illustrations of the samples obtained in the current work

sanction order No.: SB/S2/CMP-059/2013, SRG/2020/001737 and VIT SEED GRANT.

Compliance with ethical standards

Conflict of interest Authors declare no competing financial interest.

Supplementary Information: The online version contains supplementary material available at <http://doi.org/10.1007/s10854-021-05520-6>.

References

- M. Fiebig, T. Lottermoser, D. Meier, M. Trassin, The evolution of multiferroics. *Nat. Rev. Mater.* **1**, 16046 (2016)
- X. Yang, Z. Zhou, T. Nan, Y. Gao, G.M. Yang, M. Liu, N.X. Sun, Recent advances in multiferroic oxide heterostructures and devices. *J. Mater. Chem. C* **4**, 234–243 (2016)
- R. Guo, L. Fang, W. Dong, F. Zheng, M. Shen, Enhanced photocatalytic activity and ferromagnetism in Gd doped BiFeO₃ nanoparticles. *J. Phys. Chem. C* **114**, 21390–21396 (2010)
- G. Catalan, J.F. Scott, Physics and applications of bismuth ferrite. *Adv. Mater.* **21**, 2463–2485 (2009)
- W. Eerenstein, N.D. Mathur, J.F. Scott, Multiferroic and magnetoelectric materials. *Nature* **442**, 759 (2006)
- D.P. Dutta, O.D. Jayakumar, A.K. Tyagi, K.G. Girija, C.G.S. Pillai, G. Sharma, Effect of doping on the morphology and multiferroic properties of BiFeO₃ nanorods. *Nanoscale* **2**, 1149–1154 (2010)
- T.D. Rao, T. Karthik, A. Saket, Investigation of structural, magnetic and optical properties of rare earth substituted bismuth ferrite. *J. Rare Earths* **31**, 370–375 (2013)
- T. Gao, Z. Chen, Q. Huang, F. Niu, X. Huang, L. Qin, Y. Huang, A. Review, Preparation of bismuth ferrite nanoparticles and its applications in visible-light induced photocatalyses. *Rev. Adv. Mater. Sci.* **40**, 97–109 (2015)
- J. Wang, J.B. Neaton, H. Zheng, V. Nagarajan, S.B. Ogale, B. Liu, D. Viehland, V. Vaithyanathan, D.G. Schlom, U.V. Waghmare, N.A. Spaldin, K.M. Rabe, M. Wuttig, R. Ramesh, Epitaxial BiFeO₃ multiferroic thin film heterostructures. *Science* **299**, 1719–1722 (2003)
- T. Gao, Z. Chen, F. Niu, D. Zhou, Q. Huang, Y. Zhu, L. Qin, X. Sun, Y. Huang, Shape-controlled preparation of bismuth ferrite by hydrothermal method and their visible-light degradation properties. *J. Alloy Compd.* **648**, 564–570 (2015)
- T. Gao, Z. Chen, Y. Zhu, F. Niu, Q. Huang, L. Qin, X. Sun, Y. Huang, Synthesis of BiFeO₃ nanoparticles for the visible-light induced photocatalytic property. *Mater. Res. Bull.* **59**, 6–12 (2014)
- R. Safi, H. Shokrollahi, Physics, chemistry and synthesis methods of nanostructured bismuth ferrite (BiFeO₃) as a ferroelectro-magnetic material. *Prog. Solid State Chem.* **40**, 6–15 (2012)
- C.H. Yang, D. Kan, I. Takeuchi, V. Nagarajan, J. Seidel, Doping BiFeO₃: approaches and enhanced functionality. *Phys. Chem. Chem. Phys.* **14**, 15953–15962 (2012)
- N. Jeon, D. Rout, I.W. Kim, S.J.L. Kang, Enhanced multiferroic properties of single-phase BiFeO₃ bulk ceramics by Ho doping. *Appl. Phys. Lett.* **98**, 072901 (2011)
- A.I. Iorgu, F. Maxim, C. Matei, L.P. Ferreira, P. Ferreira, M.M. Cruz, D. Berger, Fast synthesis of rare-earth (Pr³⁺, Sm³⁺, Eu³⁺ and Gd³⁺) doped bismuth ferrite powders with enhanced magnetic properties. *J. Alloy Compd.* **629**, 62–68 (2015)
- Y. Li, H.J. Yang, W.G. Yang, Z.L. Hou, J.B. Li, H.B. Jin, J. Yuan, M.S. Cao, Structure, ferromagnetism and microwave absorption properties of La substituted BiFeO₃ nanoparticles. *Mater. Lett.* **111**, 130–133 (2013)
- J. Zhang, Y.J. Wu, X.K. Chen, X.J. Chen, Structural evolution and magnetization enhancement of Bi_{1-x}Tb_xFeO₃. *J. Phys. Chem. Solids* **74**, 849–853 (2013)
- B. Bhushan, A. Basumallick, S.K. Bandopadhyay, N.Y. Vasanthacharya, D. Das, Effect of alkaline earth metal doping on thermal, optical, magnetic and dielectric properties of BiFeO₃ nanoparticles. *J. Phys. D* **42**, 065004 (2009)

19. M. Li, M. Ning, Y. Ma, Q. Wu, C.K. Ong, Room temperature ferroelectric, ferromagnetic and magnetoelectric properties of Ba-doped BiFeO₃ thin films. *J. Phys. D* **40**, 1603 (2007)
20. A. Chaudhuri, K. Mandal, Study of structural, ferromagnetic and ferroelectric properties of nanostructured barium doped Bismuth Ferrite. *J. Magn. Magn. Mater.* **353**, 57–64 (2014)
21. D. Rubi, F. Gomez-Marlasca, P. Bonville, D. Colson, P. Levy, Resistive switching in ceramic multiferroic Bi_{0.9}Ca_{0.1}FeO₃. *Phys. B* **407**, 3144–3146 (2012)
22. T. Hussain, S.A. Siddiqi, S. Atiq, M.S. Awan, Induced modifications in the properties of Sr doped BiFeO₃ multiferroics. *Progr. Nat. Sci.* **23**, 487–492 (2013)
23. B. Guo, H. Deng, X. Zhai, W. Zhou, X. Meng, G. Weng, S. Chen, P. Yang, J. Chu, Cr doping-induced structural phase transition, optical tuning and magnetic enhancement in BiFeO₃ thin films. *Mater. Lett.* **186**, 198–201 (2017)
24. M. Nadeem, W. Khan, S. Khan, S. Husain, A. Ansari, Tailoring dielectric properties and multiferroic behavior of nanocrystalline BiFeO₃ via Ni doping. *J. Appl. Phys.* **124**, 164105 (2018)
25. M.S. Bernardo, T. Jardiel, M. Peiteado, F.J. Mompean, M. Garcia-Hernandez, M.A. Garcia, M. Villegas, A.C. Caballero, Intrinsic compositional inhomogeneities in bulk Ti-doped BiFeO₃: microstructure development and multiferroic properties. *Chem. Mater.* **25**, 1533–1541 (2013)
26. H.B. Sharma, N.B. Singh, K.N. Devi, J.H. Lee, S.B. Singh, Structural and optical properties of manganese substituted nanocrystalline bismuth ferrite thin films by sol–gel process. *J. Alloy. Compd.* **583**, 106–110 (2014)
27. A. Kumar, K.L. Yadav, Magnetic, magnetocapacitance and dielectric properties of Cr doped bismuth ferrite nanoceramics. *Mater. Sci. Eng. B* **176**, 227–230 (2011)
28. P.R. Vanga, R.V. Mangalaraja, N.V. Giridharan, M. Ashok, Influence of divalent Ni and trivalent Cr ions on the properties of ytterbium modified bismuth ferrite. *J. Alloy. Compd.* **684**, 55–61 (2016)
29. W. Mao, X. Wang, Y. Han, Y. Li, Y. Wang, Y. Ma, X. Feng, T. Yang, J. Yang, W. Huang, Effect of Ln (Ln= La, Pr) and Co co-doped on the magnetic and ferroelectric properties of BiFeO₃ nanoparticles. *J. Alloy. Compd.* **584**, 520–523 (2014)
30. K.G. Yang, Y.L. Zhang, S.H. Yang, B. Wang, Structural, electrical, and magnetic properties of multiferroic Bi_{1-x}La_xFe_{1-y}Co_yO₃ thin films. *J. Appl. Phys.* **107**, 124109 (2010)
31. G. Dong, G. Tan, W. Liu, A. Xia, H. Ren, Crystal structure and highly enhanced ferroelectric properties of (Tb, Cr) co-doped BiFeO₃ thin films fabricated by a sol–gel method. *Ceram. Int.* **40**, 1919–1925 (2014)
32. M. Gowrishankar, D.R. Babu, S. Madeswaran, Effect of Gd–Ti co-substitution on structural, magnetic and electrical properties of multiferroic BiFeO₃. *J. Magn. Magn. Mater.* **418**, 54–61 (2016)
33. S. Irfan, L. Li, A.S. Saleemi, C.W. Nan, Enhanced photocatalytic activity of La³⁺ and Se⁴⁺ co-doped bismuth ferrite nanostructures. *J. Mater. Chem. A* **5**, 11143–11151 (2017)
34. S. Chauhan, M. Kumar, S. Chhoker, S.C. Katyal, M. Singh, Substitution driven structural and magnetic transformation in Ca-doped BiFeO₃ nanoparticles. *RSC Adv.* **6**, 43080–43090 (2016)
35. A. Agarwal, P. Aghamkar, V. Singh, O. Singh, A. Kumar, Structural transitions and multiferroicity in Ba and Co substituted nanosized bismuth ferrite. *J. Alloy. Compd.* **697**, 333–340 (2017)
36. S. Goswami, D. Bhattacharya, P. Choudhury, B. Ouladdiaf, T. Chatterji, Multiferroic coupling in nanoscale BiFeO₃. *Appl. Phys. Lett.* **99**, 073106 (2011)
37. X.J. Xi, S.Y. Wang, W.F. Liu, H.J. Wang, F. Guo, X. Wang, J. Gao, D.J. Li, Enhanced magnetic and conductive properties of Ba and Co co-doped BiFeO₃ ceramics. *J. Magn. Magn. Mater.* **355**, 259–264 (2014)
38. R.D. Shannon, Revised effective ionic radii and systematic studies of interatomic distances in halides and chalcogenides. *Acta Crystallographica Sect. A* **32**, 751–767 (1976)
39. M.M. Rhaman, M.A. Matin, M.N. Hossain, F.A. Mozahid, M.A. Hakim, M.H. Rizvi, M.F. Islam, Band gap tuning of Sm and Co co-doped BFO nanoparticles for photovoltaic application. *J. Electron. Mater.* **47**, 6954–6958 (2018)
40. Y. Huo, Y. Jin, Y. Zhang, Citric acid assisted solvothermal synthesis of BiFeO₃ microspheres with high visible-light photocatalytic activity. *J. Mol. Catal. A* **331**, 15–20 (2010)
41. S. Chandel, P. Thakur, M. Tomar, V. Gupta, A. Thakur, Investigation of structural, optical, dielectric and magnetic studies of Mn substituted BiFeO₃ multiferroics. *Ceram. Int.* **43**, 13750–13758 (2017)
42. D. Varshney, A. Kumar, K. Verma, Effect of A site and B site doping on structural, thermal, and dielectric properties of BiFeO₃ ceramics. *J. Alloy. Compd.* **509**, 8421–8426 (2011)
43. B.K. Vashisth, J.S. Bangruwa, A. Beniwal, S.P. Gairola, A. Kumar, N. Singh, V. Verma, Modified ferroelectric/magnetic and leakage current density properties of Co and Sm co-doped bismuth ferrites. *J. Alloy. Compd.* **698**, 699–705 (2017)
44. V. Verma, Structural, electrical and magnetic properties of rare-earth and transition element co-doped bismuth ferrites. *J. Alloy. Compd.* **641**, 205–209 (2015)
45. S.S. Rajput, R. Katoch, K.K. Sahoo, G.N. Sharma, S.K. Singh, R. Gupta, A. Garg, Enhanced electrical insulation and ferroelectricity in La and Ni co-doped BiFeO₃ thin films. *J. Alloy. Compd.* **621**, 339–344 (2015)

46. H. Dai, R. Xue, Z. Chen, T. Li, J. Chen, H. Xiang, Effect of Eu, Ti co-doping on the structural and multiferroic properties of BiFeO₃ ceramics. *Ceram. Int.* **40**, 15617–15622 (2014)
47. T.J. Park, G.C. Papaefthymiou, A.J. Viescas, A.R. Moodenbaugh, S.S. Wong, Size-dependent magnetic properties of single-crystalline multiferroic BiFeO₃ nanoparticles. *Nano Lett.* **7**, 766–772 (2007)
48. A.K. Jena, S. Satapathy, J.R. Mohanty, Magnetic properties and oxygen migration induced resistive switching effect in Y substituted multiferroic bismuth ferrite. *Phys. Chem. Chem. Phys.* **21**, 15854–15860 (2019)
49. A. Puhan, A.K. Nayak, B. Bhushan, S. Praharaj, S.S. Meena, D. Rout, Enhanced electrical, magnetic and optical behaviour of Cr doped Bi_{0.98}Ho_{0.02}FeO₃ nanoparticles. *J. Alloys Compd.* **796**, 229–236 (2019)
50. P. Godara, A. Agarwal, N. Ahlawat, S. Sanghi, R. Dahiya, Crystal structure transformation, dielectric and magnetic properties of Ba and Co modified BiFeO₃ multiferroic. *J. Alloy Compd.* **594**, 175–181 (2014)
51. T. Wang, Q. Ma, S.H. Song, Highly enhanced magnetic properties of BiFeO₃ nanopowders by aliovalent element Ba-Zr co-doping. *J. Magn. Magn. Mater.* **465**, 375–380 (2018)
52. G.S. Lotey, N.K. Verma, Multiferroic properties of Tb-doped BiFeO₃ nanowires. *J. Nanoparticle Res.* **15**, 1553 (2013)
53. S. Layek, S. Saha, H.C. Verma, Preparation, structural and magnetic studies on BiFe_{1-x}Cr_xO₃ (x= 0.0, 0.05 and 0.1) multiferroic nanoparticles. *AIP Adv.* **3**, 032140 (2013)
54. A.K. Nayak, Y. Sohn, D. Pradhan, Facile green synthesis of WO₃·H₂O nanoplates and WO₃ nanowires with enhanced photoelectrochemical performance. *Cryst. Growth Des.* **17**, 4949–4957 (2017)
55. S. Irfan, S. Rizwan, Y. Shen, L. Li, S. Butt, C.W. Nan, The gadolinium (Gd³⁺) and Tin (Sn⁴⁺) Co-doped BiFeO₃ nanoparticles as new solar light active photocatalyst. *Sci. Rep.* **7**, 42493 (2017)
56. M. Hasan, M.A. Basith, M.A. Zubair, M.S. Hossain, R. Mahbub, M.A. Hakim, M.F. Islam, Saturation magnetization and band gap tuning in BiFeO₃ nanoparticles via co-substitution of Gd and Mn. *J. Alloy Compd.* **687**, 701–706 (2016)
57. R. Viswanatha, D.D. Sarma, Study of the growth of capped ZnO nanocrystals a route to rational synthesis. *Chemistry* **12**, 180 (2006)
58. P. Kumar, M. Kar, Effect of structural transition on magnetic and optical properties of Ca and Ti co-substituted BiFeO₃ ceramics. *J. Alloy Compd.* **584**, 566–572 (2014)
59. P. Machado, M. Scigaj, J. Gazquez, E. Rueda, A. Sánchez-Díaz, I. Fina, M. Gibert-Roca, T. Puig, X. Obradors, M. Campoy-Quiles, M. Coll, Band gap tuning of solution-processed ferroelectric perovskite BiFe_{1-x}Co_xO₃ Thin Films. *Chem. Mater.* **31**, 947–954 (2019)
60. S. Chakraborty, M. Pal, Highly efficient novel carbon monoxide gas sensor based on bismuth ferrite nanoparticles for environmental monitoring. *New J. Chem.* **42**, 7188–7196 (2018)
61. M. Mousavi, A. Habibi-Yangjeh, M. Abitorabi, Fabrication of novel magnetically separable nanocomposites using graphitic carbon nitride, silver phosphate and silver chloride and their applications in photocatalytic removal of different pollutants using visible-light irradiation. *J. Colloid Interface Sci.* **480**, 218–231 (2016)
62. C. Xu, P.R. Anusuyadevi, C. Aymonier, R. Luque, S. Marre, Nanostructured materials for photocatalysis. *Chem. Soc. Rev.* **48**, 3868 (2019)
63. X. Yang, Z. Chen, J. Fang, Q. Yang, W. Zhao, X. Qian, D. Zhou, C. Liu, M. Chen, Freestanding 3D MoS₂ nanosheets/graphene aerogel heterostructure as a recyclable photocatalyst for efficiently degrading antibiotic residues. *Mater. Lett.* **252**, 5–7 (2019)
64. X. Yang, Z. Chen, D. Zhou, W. Zhao, X. Qian, Q. Yang, T. Sun, C. Shen, Ultra-low Au–Pt Co-decorated TiO₂ nanotube arrays: Construction and its improved visible-light-induced photocatalytic properties. *Sol. Energy Mater. Sol. Cells* **201**, 110065 (2019)
65. F. Gao, X.Y. Chen, K.B. Yin, S. Dong, Z.F. Ren, F. Yuan, T. Yu, Z.G. Zou, J.M. Liu, Visible-light photocatalytic properties of weak magnetic BiFeO₃ nanoparticles. *Adv. Mater.* **19**, 2889–2892 (2007)
66. Y.K. Abdel-Monem, S.M. Emam, H.M. Okda, Solid state thermal decomposition synthesis of CuO nanoparticles from coordinated pyrazolopyridine as novel precursors. *J. Mater. Sci.* **28**, 2923–2934 (2017)
67. M. Madkour, Y.K. Abdel-Monem, F. AlSagheer, Controlled synthesis of NiO and Co₃O₄ nanoparticles from different coordinated precursors: impact of precursor's geometry on the nanoparticles characteristics. *Ind. Eng. Chem. Res.* **55**, 12733–12741 (2016)
68. A. Bumajdad, M. Madkour, Y. Abdel-Moneam, M. El-Kemary, Nanostructured mesoporous Au/TiO₂ for photocatalytic degradation of a textile dye: the effect of size similarity of the deposited Au with that of TiO₂ pores. *J. Mater. Sci.* **49**, 1743–1754 (2014)
69. F. Azeez, E. Al-Hetlani, M. Arafá, Y. Abdelmonem, A.A. Nazeer, M.O. Amin, M. Madkour, The effect of surface charge on photocatalytic degradation of methylene blue dye using chargeable titania nanoparticles. *Sci. Rep.* **8**, 1–9 (2018)
70. H.S. Mandour, A.A. Nazeer, E. Al-Hetlani, M. Madkour, Y.K. Abdel-Monem, Organic nanoparticles of acetohydrazides as novel inhibitors for mild steel corrosion. *New J. Chem.* **42**, 5914–5922 (2018)

71. Y.K. Abdel-Monem, Efficient nanophotocatalyt of hydrothermally synthesized Anatase TiO_2 nanoparticles from its analogue metal coordinated precursor. *J. Mater. Sci.* **27**, 5723–5728 (2016)
72. A.K. Nayak, S. Lee, Y. Sohn, D. Pradhan, Biomolecule-assisted synthesis of $\text{In}(\text{OH})_3$ nanocubes and In_2O_3 nanoparticles: photocatalytic degradation of organic contaminants and CO oxidation. *Nanotechnology* **26**, 485601 (2015)

Publisher's Note Springer Nature remains neutral with regard to jurisdictional claims in published maps and institutional affiliations.